



Combined ERT and borehole logs for mapping the soil-rock interface in a granitic environment

Adedibu Sunny Akingboye^{1, 2}  and Andy Anderson Bery¹ 

¹ School of Physics, Universiti Sains Malaysia, Penang, Malaysia

² Department of Earth Sciences, Adekunle Ajasin University, Akungba-Akoko, Ondo State, Nigeria

Received 15 March 2022, in final form 27 October 2022

This study used the efficiency of electrical resistivity tomography (ERT) and borehole logs to map the soil-rock interface beneath four traverses (RS1, RS2, RS3, and RS4) in the granitic terrain of Perak, Peninsular Malaysia. The study aimed to evaluate the impacts of the soil-rock characteristic features and interfaces on groundwater and infrastructure development to meet the needs of the increasing inhabitants yearly. The borehole- and ERT-derived lithologic units are strongly correlated. The delineated lithologic units include the topsoil, weathered granitic units (medium stiff to hard silty clay or clayey silt with $< 800 \Omega\text{m}$), thin to wide-sized weathered/fractured units, and fresh granitic bedrock. These soil-rock profiles and weathered/fractured apertures support sustainable groundwater developments with drill depths above 45 m. In contrast, the delineated clay/silt alternating with stiffer soils, low load-bearing deep-weathered/fractured zones, and bedrock boulders in most places, except beneath traverse RS3, have high affinities for water retention and differential stresses. These features can adversely impact poorly reinforced foundations. Hence, structural elements of the foundations, such as footings or piles, should be placed on stable bedrock, particularly in the central to western parts of the study area. This study has reduced the paucity of information on using ERT and borehole logs for soil-rock interface studies in the study area.

Keywords: soil-rock resistivity, borehole logs, soil-rock interface, granitic terrain, hydrogeophysics, geoen지니어ing study

1. Introduction

In granitic environments, like other terranes, denudation and high infiltration processes can result in complex soil profiles due to varying weathering conditions (Bery and Saad, 2012; Cheng et al., 2019). Over the years, surficial and subsurface soil-rock characterizations have significantly improved through

advances in geophysical data imaging methods, data processing algorithms, and modeling. Of all the geophysical methods, electrical resistivity tomography (ERT) has emerged as an effective imaging technique for soil-rock characterizations and several subsurface studies. ERT provides georesistivity characteristics related to lithologic units, geologic structures, groundwater, and geoengineering properties of the subsurface formation, among others (Storz et al., 2000; Akingboye et al., 2022a). It is suitable for rapid and detailed mapping of soil-rock profiles, interfaces, and associated geologic structures (Bery and Saad, 2012; Cheng et al., 2019; Hasan et al., 2020).

Soil-rock interface is a common contact form, widely distributed in various geological environments, and involves many fields, presenting different structures and characteristics (Cheng et al., 2019; Yang et al., 2020). In addition, infrastructure will inevitably encounter soil-rock interface, and geoengineering problems are consequent (Ganerød et al., 2006; Akingboye et al., 2020; Hasan et al., 2022). Via soil-rock interface evaluation, geoengineering problems such as landslides, ground subsidence, soil liquefaction, etc., can be predicted based on the degree of water saturation and unconsolidated soils (Yalcinkaya et al., 2016). On the other hand, inaccurate delineation could make groundwater exploration difficult.

Consequently, soil-rock resistivity is pertinent in accurately delineating the soil-rock interface (Cheng et al., 2019). The technique can also indirectly evaluate the properties and compositions of soils, such as moisture, salinity, porosity, organic matter level, bulk density, and soil texture, and in delineating concealed geologic structures, including weathered troughs, open-to-surface fractures, air- or water-filled voids, etc (Laloy et al., 2011; Aizebeokhai, 2014; Akingboye and Osazuwa, 2021; Akingboye et al., 2022a; Akingboye and Bery, 2022). Integrating borehole litho logs with soil-rock resistivity models can enhance the accurate delineation of these subsurface geologic parameters. However, borehole drilling comes at a high cost and delayed operational time. As a result, soil-rock interface, in conjunction with other lithological properties, is vital in understanding subsurface geodynamics, environmental and ecological processes, and the impacts of natural and anthropogenic-driven changes on the ecosystems (Chalikakis et al., 2011; Cheng et al., 2019; Akingboye and Bery, 2021a; Akingboye et al., 2022a). It is also relevant in evaluating water-rock interaction (Stober and Bucher, 2015a, 2015b), groundwater potential (Arora et al., 2016; Gao et al., 2018; Christensen et al., 2020), and groundwater aquifers' vulnerability (Akintorinwa et al., 2020; Hasan et al., 2020; Akingboye et al., 2022b).

Given the above, this study employed the efficiency of the ERT and borehole logs to delineate the soil-rock interfaces in a typical granitic environment in Perak, Peninsular Malaysia. The study area is in a wet tropical region experiencing yearly torrential rainfalls and high-temperature intensity. These two factors and other geologic processes result in progressive weathering of the subsurface lithologies, producing varying subsurface soil profiles, structural features, and

soil-rock instability (Bery, 2016; Cao et al., 2020; Akingboye and Bery, 2021a, 2021b, 2022). This study is crucial because soil-rock interfaces are potentially problematic concerning groundwater inflow, especially in complex geological terrains, due to the lithological properties, stress regimes, and morphological differences, *e.g.*, (Eriksson, 2014; Yang et al., 2020). Understanding the soil-rock interface provides detailed insights into the nature, geometry, architecture, and hydrogeologic potential of the subsurface soil-rock profiles. These are significant for groundwater prospecting and infrastructure design to meet the increasing yearly needs of the study area's inhabitants. In addition, the study will substantially reduce the paucity of information on hydrogeophysics/hydro-geology and engineering characteristics of the soil-rock profiles in the study area.

2. Geological setting of the study area

Peninsular Malaysia is located at the southeast margin of the Eurasian continent. It was formed by the amalgamation of the Sibumasu Block and Indo-China Block along the Bentong-Raub suture (Fig. 1a) during the Permian-Triassic (Metcalfe, 2000, 2001; Ng et al., 2015a, 2015b; Cao et al., 2020). The collisional event resulted in the closure of the Paleo-Tethys Ocean Basin, and the remnants of the basin were preserved in the Bentong-Raub Suture (Metcalfe, 2000). Peninsular Malaysia is subdivided into three belts: Western, Central, and Eastern Belts, as shown in Fig. 1a, based on the boundaries and trends of the Bentong-Raub and Lebir faults. The Central Belt comprises a Carboniferous-Permian sequence of limestone, shale (with subordinate sandstone), siltstone, and conglomerate (Schwartz et al., 1995). The Eastern Belt in the Indo-China domain consists of the Malaysian granitoids of Permian to Late Triassic I-type granites, typically biotite granites. On the other hand, the Late Triassic S-type granites, typically biotite granite and granodiorite, are the noticeable rocks in the Western and Central Belts of the Sibumasu domain, respectively (Ng et al., 2015a). The S-type granites of the Western and Central Belts and the I-type granites of the Eastern Belt were formed by the partial melting of the Sibumasu Block and the Indo-China Block (Ng et al., 2015a; 2015b; Cao et al., 2020). These granitoids are typical of two granite belts: the Main Range Granite Province (MRGP) and the Eastern Granite Province (EGP), bounded by the Bentong-Raub Suture. Generally, the area's approximately N–S trending faults are widespread due to the collision of the Sibumasu and Indo-China Blocks (Abdullah and Purwanto, 2001).

The study area is located in Hulu Perak State, Malaysia, between latitudes 5°11'54.24" N and 5°11'57.63" N and longitudes 101°23'43.91"E and 101°23'53.81" E (Fig. 1b–c). Hulu Perak is Perak State's largest district. It is bordered on the east by Kelantan, on the west by Kedah, Kuala Kangsar district to the south, and the communities of Larut, Matang, and Selama are on the southwest. Perak also shares a border with the Betong District of Thailand. The

study area is located on the MRGP. Perak's geology is divided into four major parts (Fig. 1b). The Quaternary formation comprises marine and continental deposits, such as clay, silt, sand, and peat with minor gravel and basalt of early Pleistocene age, covering 24% of the study area. The Triassic-Jurassic sedimentary rocks of marine origin form a wide belt in the area. These rocks include

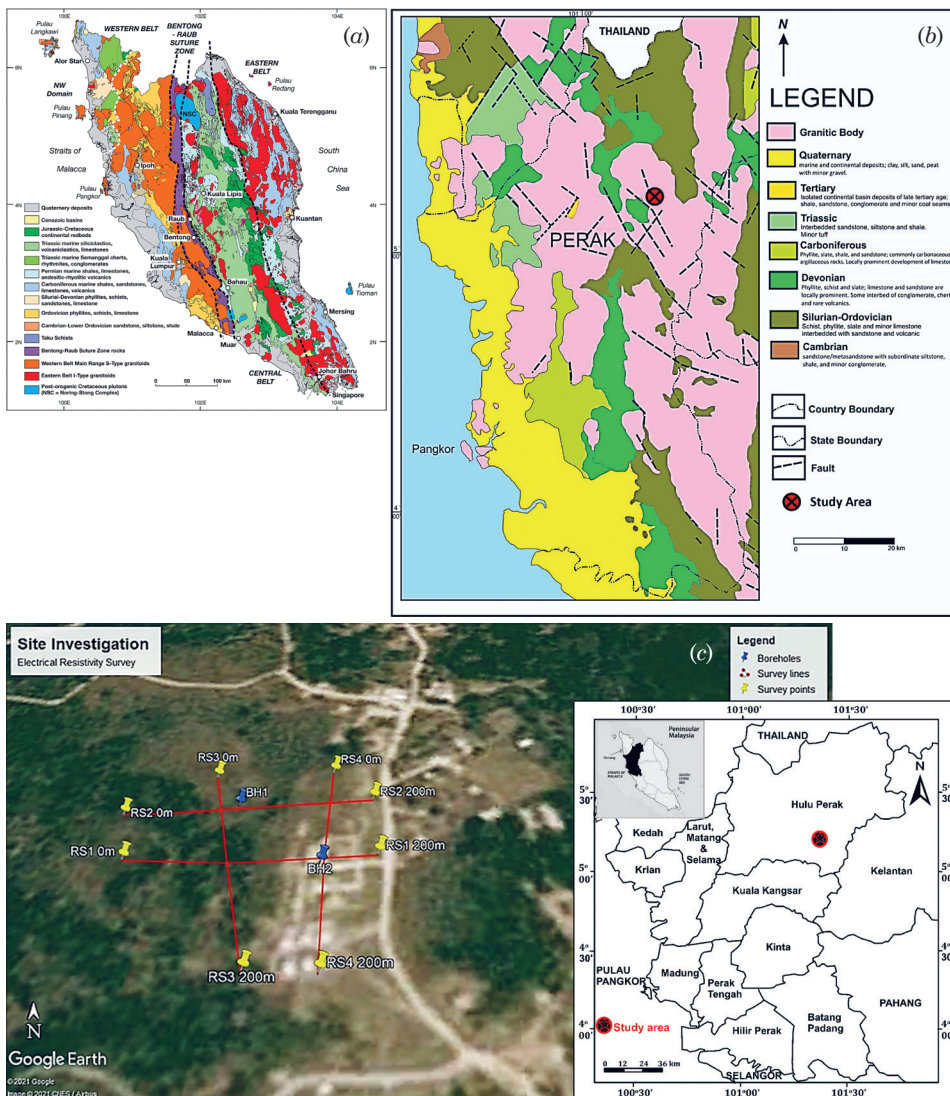


Figure 1. (a) Simplified regional geological map of Peninsular Malaysia, after (Tate et al., 2009). (b) Geological map of Perak and its environs (after bin Kamaruzzaman et al., 2020). (c) Aerial acquisition map of the study area. Inset: Location map of Perak State, Malaysia.

shale, mudstone, siltstone, sandstone, and minor limestone lenses. Interbeds of tuff are also common within this openly crumpled sequence, covering 15% of the study area. The Silurian formation consists of tightly compressed consolidated shale, slate, argillite, metasandstone, phyllite, and schist. These rocks are about 16% of the study area. Finally, the intrusive rocks, mainly undifferentiated igneous rocks of granitic origin, cover 45% of the study area (Lee et al., 2004; bin Kamaruzzaman et al., 2020; Nuhu et al., 2021). The studied section is underlain by typical granite.

3. Methodology

3.1. Geophysical ERT field measurements

A total of four ERT traverses, indicated as RS1, RS2, RS3, and RS4, were covered using a spread length of 200 m each with a 5 m electrode spacing to measure the subsurface resistivity variations in the study area. RS1 and RS2 were established roughly W–E, while RS4 was approximately in N–S, deviating slightly from RS3 in the same direction. Instead of the small electrode spacing required for engineering surveys, the employed electrode spacing ensures deeper probing depth and adequate mapping of the deep bedrock structures. That way, the deep aquifer units supporting groundwater conduits and storage, as well as high-risk near-surface soil-rock profiles to infrastructure design, were adequately delineated.

The resistivity values of subsurface lithologic units were measured using the ABEM SAS 4000 Resistivity Meter with its accessories, employing the Wenner-Schlumberger array. The Wenner-Schlumberger array has a more considerable median depth of investigation and is sensitive to horizontal and vertical structures. Hence, it can optimize the signal-to-noise ratio to achieve a high-resolution inverse resistivity model with significantly little or no distorted structural artifacts (Loke and Lane, 2004; Akingboye and Ogunyele, 2019; Akingboye and Bery, 2022). Two boreholes (BH1 and BH2) were drilled at the station distances of 110 m on RS2 and RS4 (Fig. 1c), with maximum depths of 11 m and 12.25 m, respectively. BH1 and BH2 were very close to RS3 and RS1, allowing for determining the true nature of the subsurface lithologic units and their respective depths. The ERT models leveraged the borehole-derived logs to resolve the ambiguities/uncertainties in resistivity and thickness values of penetrated layers.

3.2. Geophysical field data processing, inversion, and modeling

The field ERT data sets were processed and iteratively inverted using the RES2DINV software by employing the least-squares inversion approach (Loke and Barker, 1996; Loke, 2004). The used linearized smoothness-constrained least-squares optimization method, as given in Eq. 1, provides the relationship

between the model parameters (r) and the data misfit (g), *e.g.*, (DeGroot-Hedlin and Constable, 1990; Loke, 2004; Dahlin and Loke, 2018).

$$\left[J_i^T R_d J_i + \lambda_i W^T R_m W \right] \Delta r_i = J_i^T R_d g_i - \lambda_i W^T R_m W r_{i-1} \quad (1)$$

J is the Jacobian matrix that contains the logarithms of the apparent resistivity measurements with respect to the model resistivity values; W is the roughness filter, and λ is the damping factor. g is the data misfit vector that contains the difference between the logarithmic measured and calculated resistivity values. Δr_i is the required change in the model parameters for the iterations that will reduce the data misfit. $r_{(i-1)}$ is the resistivity model of the previous iteration. R_d and R_m are the weighting matrices used by the robust inversion method.

Furthermore, the finite-element method of 4 nodes with L2-norm was used as the least-squares constraint to minimize the difference between the calculated and observed apparent resistivities. A damping factor of 0.05, with a minimum value of 0.01, was used to increase the accuracy and resolution of the calculated and observed resistivity models. According to Cheng et al. (2019), measurement and modeling errors can significantly impact the computed resistivity model of real-time field data sets. Hence, each ERT model's root mean square error (RMSE) was monitored for the true subsurface resistivity distribution. According to Loke (2004), it is essential to note that an inverted resistivity model with the lowest RMSE may sometimes not give the ideal subsurface geological structures and anomalies. It is also worth noting that the accurate delineation of the soil-rock interface decreases with increasing measurement error. This is a key factor in the quantitative assessment of soil-rock interface mapping (Cheng et al., 2019; Akingboye and Bery, 2021a, b). As a result, the 7th iteration was considered the best for the RMSE convergence. At this iteration level, the inverse model resistivity section yielded significantly no or minor changes in error values, giving the most realistic subsurface geological characteristics comparable with the borehole logs.

4. Results

The generated resistivity distribution patterns for the measured and calculated apparent resistivity pseudosections are practically identical, as depicted in Fig. 2. The integration of borehole logs (Fig. 3) with ERT models shows a strong lithological correlation. The borehole-derived logs effectively resolve the difficulties in identifying low-resistive lithologic materials and differentiating water-saturated zones from clay/silt. Generally, the borehole-derived lithologic units consisting of topsoil, weathered layer (medium stiff to hard silty clay or clayey silt), weathered/fractured bedrock, and fresh granitic bedrock are characterized by resistivity values of $< 1000 \Omega\text{m}$, < 10 to $800 \Omega\text{m}$, < 50 to $< 1000 \Omega\text{m}$, and $> 1000 \Omega\text{m}$, respectively.

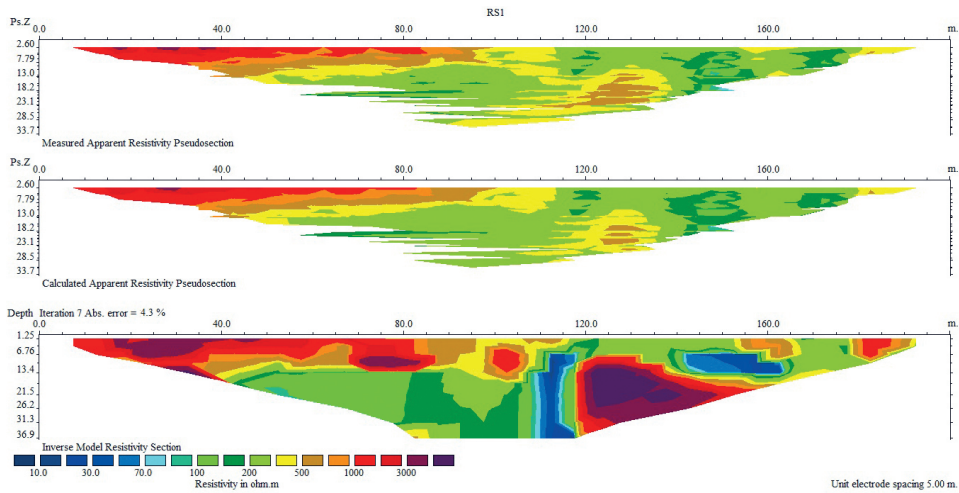


Figure 2. 2D ERT composite model of the measured (*top*) and calculated resistivity pseudosections (*middle*) and inverse model resistivity section (*bottom*) of RS1.

Comprehensive insights into the nature of the soil-rock interfaces and architectures were gained by comparing the ERT results with the 2D simplified sub-

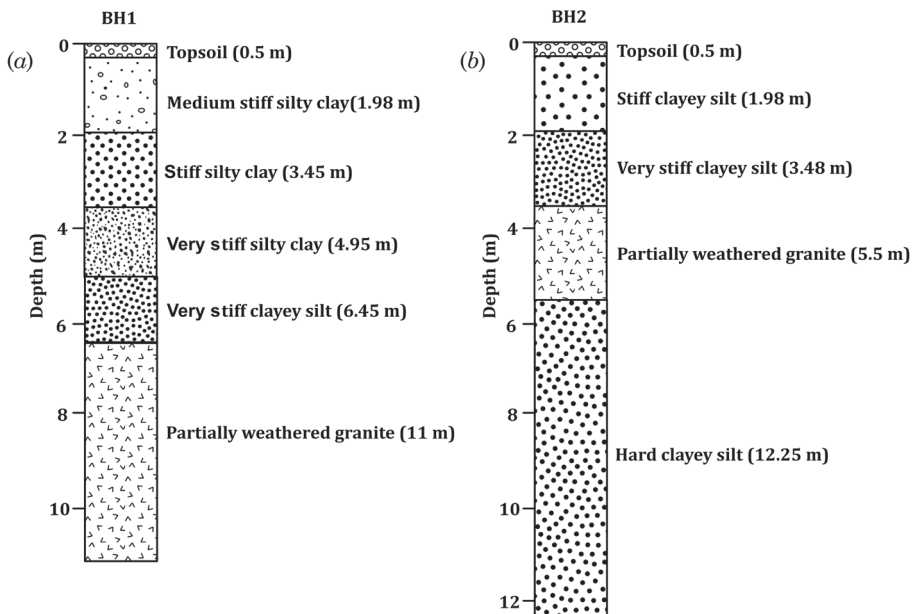


Figure 3. Subsurface lithologic units derived from (a) BH1 and (b) BH2 at the station positions of 110 m on RS1 and RS2 in the study area.

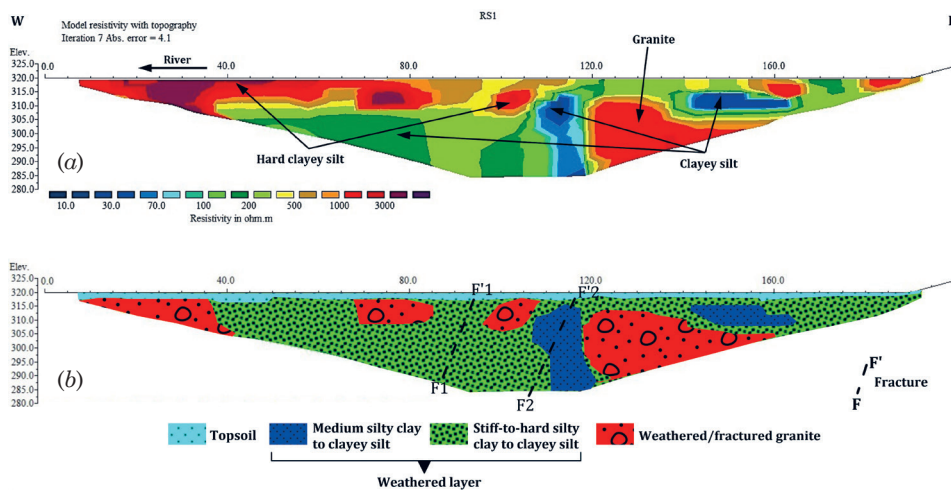


Figure 4. (a) Inverse model resistivity section and (b) the simplified subsurface geological model of RS1 with identified soil-rock interface and structures.

surface geological models of the study area. The observed resistivity anomalies in the study area were truncated by varying fractures ($F-F'$) and weathered troughs. Both features constitute the low conductive zones aside from the clayey/silty sections. The ERT model of RS1, as shown in Fig. 4a, shows that the weathered layer is characterized by clayey silt with a resistivity value of about $70 \Omega\text{m}$. A typical example is a deep-weathered trough between station positions of 95 m and 120 m. The weathered layer forms circular bodies beneath the moderately high resistive sections at the near-surface between station positions of 70–90 m and 140–165 m. The granitic bedrock beneath RS1 had undergone a series of progressive weathering and fracturing, creating floaters in the form of granitic boulders. Considering the anomalous features at the western end of RS1, as shown in Fig. 4b, the two fractures, *i.e.*, $F1-F'1$ and $F2-F'2$, delineated at stations 95 m and 120 m, respectively, must have enhanced the deep weathering of the particular section.

In Fig. 5a, the weathered layer with medium silty clay ($< 100 \Omega\text{m}$) formed two isolated low-resistive zones at depths of 10–27 m and 12.5–27 m, respectively. These features extend laterally to about 25 m and 13 m between the station positions of 65–95 m and 110–133 m, respectively. Deep-weathering mainly produced stiff silty clay ($< 800 \Omega\text{m}$) beneath RS2. Similarly, the deep-weathered zone at station points of 150–155 m is typical of stiff silty clay, with a resistivity value of about $500 \Omega\text{m}$. The weathered/fractured bedrock units beneath RS2 are similar to those delineated along RS1 (Fig. 4a–b). The laterally extensive weathered/fractured zones beneath RS2 are interspersed by resistive boulders, with dimensions ranging from 2–24 m. Also, three penetrative fractures ($F3-F'3$, $F4-F'4$, and $F5-F'5$) were identified at station positions of 65 m, 95 m, and 130 m,

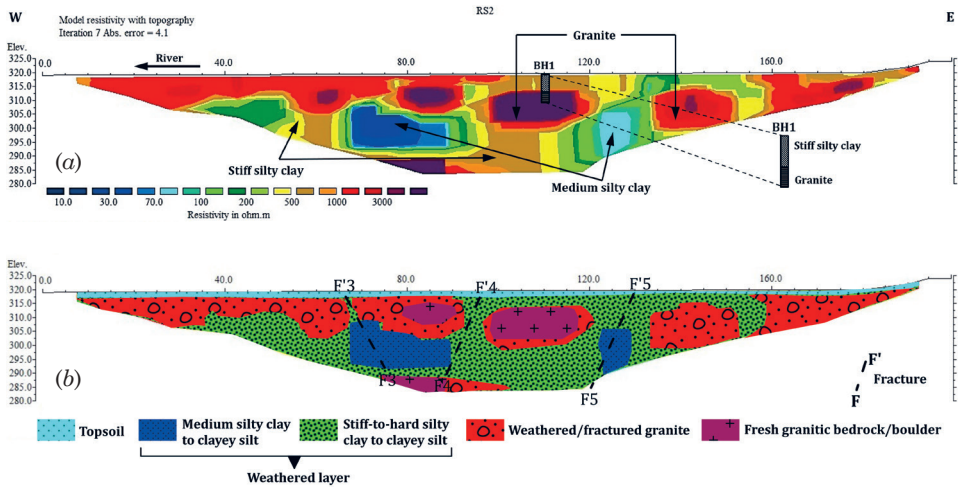


Figure 5. (a) Inverse model resistivity section and (b) the simplified subsurface geological model of RS2.

respectively (Fig. 5b). However, F3–F'3 may have been formed by tectonic stresses and the gradual weathering of the fractured bedrock.

The resistivity model in Fig. 6 shows moderate to high resistivity patterns, depicting the partially weathered to massive fresh granitic units beneath RS3 from station positions of 60 to 155 m. This massive bedrock was discontinued by deep weathering/fracturing at its two flanks, producing stiff-to-hard silty clay

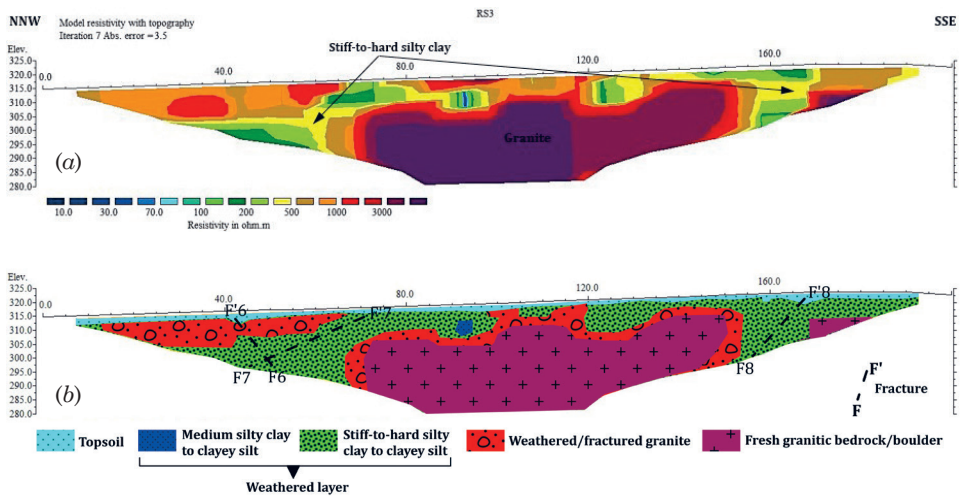


Figure 6. (a) Inverse model resistivity section and (b) the simplified subsurface geological model of RS3.

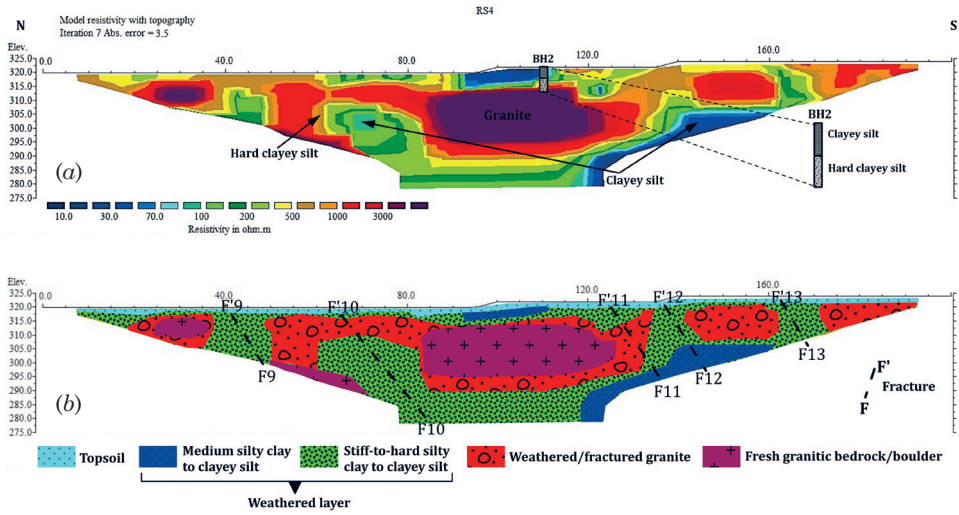


Figure 7. (a) Inverse model resistivity section and (b) the simplified subsurface geological model of RS4.

(Fig. 6a–b). Bedrock boulders and multiple fractures (F6–F’6, F7–F’7, and F8–F’8, within the station positions of 40–54 m, 65–75 m, and 150–170 m, respectively) were also delineated. Like RS3, the resistivity model beneath RS4 (Fig. 7a) depicts a large fresh granitic boulder of about 45 m in length between station positions of 82 m and 127 m. Near the surface of the granitic bedrock, at the position of BH2, the borehole-derived soil (hard clayey silt) was probably formed from the gradual weathering of the extensive granitic boulder. Multiple penetrative fractures and deep weathering also segregated the imaged large-sized granitic bedrock slab. The identified fractures (F9–F’9, F10–F’10, F11–F’11, F12–F’12, and F13–F’13) may have enhanced the weathering conditions beneath this traverse, arising from water saturation and thus produced residual clayey silt (Fig. 7a–b).

5. Discussion

5.1. Soil-rock resistivity characterization: implications for soil-rock architecture, water-rock interaction, and groundwater development

The subsurface lithologic units beneath the study area are motley topsoil, weathered layer, weathered/fractured bedrock, and fresh granitic bedrock. Generally, the topsoil’s thickness extends to a depth of about 2.0 m. In contrast, the weathered granitic units range from about 1.0 m to a depth above 45 m (deep-weathered and fractured zones). The weathered/fractured bedrock units are characterized by varying resistivities (Figs. 4–7) due to small to large-sized boulder remnants, except RS3 with massive fresh bedrock. This implies that the bedrock had significantly been deformed, arising from the progressive weather-

ing of highly susceptible bedrock minerals such as feldspars and micas (Robineau et al., 2007; Akingboye and Bery, 2022). As observed in Figs. 4–7, a total of thirteen fractures were identified and interpreted as F1–F^o1 to F13–F^o13. The observed varying resistivities are attributed to the compositions of subsurface geology and mainly clay/silt. This is because resistivity decreases with increasing clay/silt content (Hasan et al., 2020). In addition, water-rock interaction, deep-weathering, and fractures have significantly reduced the resistivity values of the subsurface lithologic units (Stober and Bucher, 2015a, 2015b). The soil-rock interfaces are flat to rugous undulating surfaces, especially the granitic bedrock occurring as small-to-extensive slabs and boulders.

To clearly understand the orientations of the delineated fractures in Figs. 4–7, a fence image for the four resistivity models was produced, representing a typical 3D subsurface resistivity geotomographic model of the study area (Fig. 8). The major fractures delineated are F1, F2, F3, and F4 (Fig. 8) based on the apertures and axial directions of the thirteen features identified in Figs. 4–7. F1, F2, and F3 orientations are approximately NE-SW, while F4 is approximately in the NW-SE direction. F2–F4 are from the same point and are connected to other fractured zones. The delineated major fractures are open-to-surface fractures, aiding water infiltration and seepages (Storz et al., 2000; Ganerød et al., 2006; Akingboye and Bery, 2022).

Considering the weathered/fractured zones beneath the study area, there is a high potential for sustainable groundwater development. The potential zones are pinned on the weathered/fractured sections in the northern, eastern, and

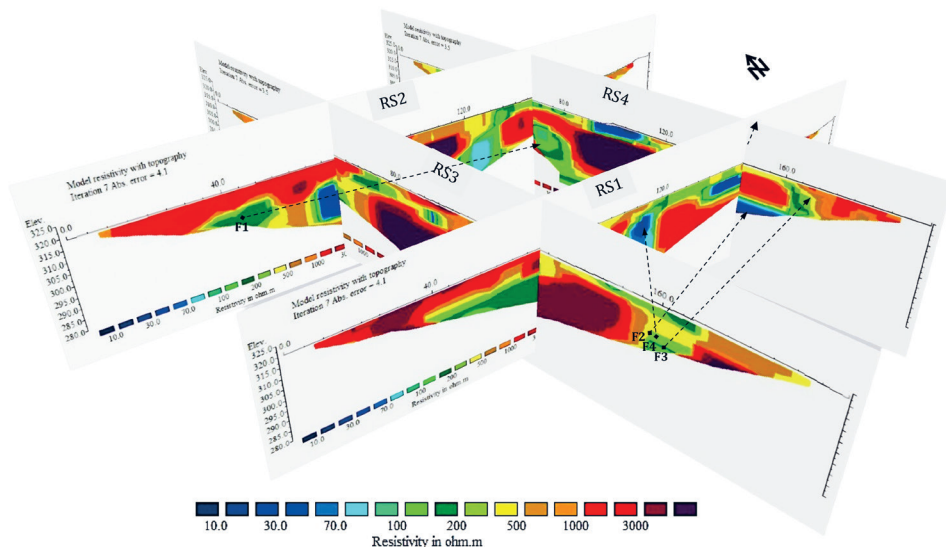


Figure 8. 3D subsurface resistivity geotomographic model of the study area. The dashed arrows labeled F1 to F4 indicate the major fractures in the study area.

southern parts with F2–F4 (Fig. 8). The probable drill depths for boreholes in this area exceed 45 m, indicating the localization of aquifers preferentially within the deep-weathered and fractured zones (Figs. 4–8). The connectivities, geometries, and apertures of the delineated soil-rock structures are significant factors in enhancing groundwater distribution and storage in the study area. These factors are closely related to weathering, fracturing, paleo and in situ stress regimes, and regional tectonic of the bedrock (Hasan et al., 2020). The massive resistive granitic bedrock outcropping at or near the surface in the central to western parts of the study area, especially beneath RS3 (see Figs. 5 and 8), may significantly reduce the groundwater potential of the area. Due to the silty/clayey nature of the subsurface weathered bodies, intended boreholes in the study area should be adequately cased to prevent occlusion.

5.2. Implications of soil-rock resistivity characterization on infrastructure design

In pre- and post-engineering constructions, understanding the implications of the observed geoelectric properties of the subsurface lithologic units and soil-rock interface on infrastructure is essential. The delineated soil profiles, typically silty clay and clayey silt, with a resistivity of about 70 Ωm at the topsoil and weathered/fractured columns (Figs. 4–8), suggest potential threats to infrastructures without reinforced foundations. Therefore, foundation failure in the study area is premised on the petrophysical, geomechanical, and hydrogeological characteristics of the near-surface soil-rock profiles, interfaces, and structures. These are the determining factors for the safety and durability of engineered structures (Akingboye and Bery, 2022; Hasan et al., 2022).

Figure 8 depicts both stable and unstable soil-rock characteristic features and interfaces. The stable sections are characterized by stiff-to-hard silty clay or clayey silt and massive granitic bedrock. On the other hand, the unstable sections comprise saturated medium silt clay or clayey silt at shallow and deep sections, including open-to-surface fractures between station positions of 55 m and 100 m, and 120 m eastward. Floaters of bedrock boulders at near-surface depths and unstable (undulating) soil-rock interface are imminent problems, especially for heavy-weight engineering structures. As a result, the placement of structural elements of the foundation, such as footings or piles on the unstable sections, could result in uncontrollable structural defects attributed to ground subsidence, tilting, cracking, etc (Yalcinkaya et al., 2016). Besides, the fine grain properties of silty clay and clayey silt, including weathered/fractured sections, have a high affinity for water retention; hence, they can adversely impact poorly reinforced foundations (Storz et al., 2000; Robineau et al., 2007; Akingboye and Bery, 2022; Hasan et al., 2020, 2022). This is because the expansion and shrinkage of the thick clayey bodies can trigger cracks in foundations due to differential settlement. Even the stiff-to-hard clayey silt bodies may hold a copious amount of water with time, resulting in foundation failures (Bery and Saad, 2012). In addi-

tion, pre-stressed and stressed clayey materials are more susceptible to subsidence due to varying environmental conditions under a long-term process of compression and stiffening, resulting in the gradual reduction of pore fluid pressure and increased effective stress (Soupios et al., 2007). Hence, proper reinforced foundations and engineering designs are required for high-rise buildings generally in the study area. Piling to the stable bedrock is recommended, particularly in eastern and northern sections with low load-bearing near-surface lithological materials (Figs. 4–8). It is recommended that infrastructure with continuous foundation footings not be placed on clayey materials alternating with stiffer soils.

6. Conclusions

This study used combined ERT and borehole logs to delineate the soil-rock interface in a typical wet tropical granitic environment in Perak, Peninsular Malaysia. The derived soil-rock resistivity models were used to evaluate the implications of the soil-rock interface and architecture on groundwater and infrastructure development. The identified borehole-derived soil-rock features strongly correlate with the ERT-derived lithologic units in the study area. The observed resistivity signatures identified the interfaces between the topsoil and weathered layer (medium stiff to hard silty clay and clayey silt) and the fresh granitic bedrock. Also, soil-rock features such as boulders, horizontal to gently dipping bedrock slabs, multiple fractures, and varying weathered troughs were delineated beneath the area.

The soil-rock architecture of the study area supports sustainable groundwater development due to the depths of soil-rock structures above 45 m, except for the western axis beneath RS3. The geometries of the aquifers are considerably wide, and the fractures are well connected to deep-weathered troughs. On a lighter note, prospective boreholes in the area may experience silty/clayey intrusion and occlusion if not adequately developed and cased. Conversely, the low subsurface load-bearing and high water retention zones require that intended infrastructure, particularly high-rise buildings, be piled to stable bedrock with reinforced foundations to prevent structural defects. Excavation of clay with alternating stiffer soils, which are pervasive at near-surface depths, should be carried out before constructing buildings with continuous footings. The massive fresh bedrock extending westward beneath RS3 is a suitable section for foundation placement in the study area. The present study has contributed significantly to the efficiency of ERT and borehole logs in soil-rock interface studies in wet tropical granitic terrains.

Acknowledgements – The authors gratefully appreciate the scientific reviews of the two anonymous reviewers, which have contributed to the manuscript's readability. The School of Physics (Geophysics Unit) is acknowledged for providing the necessary research resources for successfully executing this scientific piece.

Data Availability – All data generated or analyzed during this study are included in this published article. The corresponding author can make other supporting analyzed data available upon reasonable request.

Funding – This research received no specific grant from public, commercial, or not-for-profit funding agencies.

Declaration of competing interest – The authors declare that they have no known competing financial interests or personal relationships that could have appeared to influence the work reported in this paper.

References

- Abdullah, I. and Purwantoa, H. S. (2001): Deformational history of the Eastern Belt, Peninsular Malaysia, *Gondwana Res.*, **4**, 556.
- Aizebeokhai, A. P. (2014): Assessment of soil salinity using electrical resistivity imaging and induced polarization methods, *Afr. J. Agric. Res.*, **9**, 3369–3378, <https://doi.org/10.5897/AJAR2013.8008>.
- Akingboye, A. S. and Bery, A. A. (2022): Characteristics and rippability conditions of near-surface lithologic units (Penang Island, Malaysia) derived from multimethod geomorphologic models and geostatistics, *J. Appl. Geophys.*, **204**, 104723, <https://doi.org/10.1016/j.jappgeo.2022.104723>.
- Akingboye, A. S., Bery, A. A., Kayode, J. S., Asulewon, A. M., Bello, R. and Agbasi, O. E. (2022a): Near-surface crustal architecture and geohydrodynamics of the crystalline basement terrain of Araromi, Akungba-Akoko, SW Nigeria, derived from multi-geophysical methods, *Nat. Res. Res.*, **31**, 215–236, <https://doi.org/10.1007/s11053-021-10000-z>.
- Akingboye, A. S., Bery, A. A., Kayode, J. S., Ogunyele, A. C., Adeola, A. O., Omojola, O. O. and Adesida, A. S. (2022b): Groundwater-yielding capacity, water-rock interaction, and vulnerability assessment of typical gneissic hydrogeologic units using geoelectrohydraulic method, *Acta Geophys.*, **70**, <https://dx.doi.org/10.1007/s11600-022-00930-4>.
- Akingboye, A. S. and Bery, A. A. (2021a): Evaluation of lithostratigraphic units and groundwater potential using the resolution capacities of two different electrical tomographic electrodes at dual-spacing, *Contributions to Geophysics and Geodesy*, **51**, 295–320, <https://doi.org/10.31577/congeo.2021.51.4.1>.
- Akingboye, A. S. and Bery, A. A. (2021b): Performance evaluation of copper and stainless-steel electrodes in electrical tomographic imaging, *J. Phys. Sci.*, **32**, 13–29, <https://doi.org/10.21315/jps2021.32.3.2>.
- Akingboye, A. S. and Osazuwa, I. B. (2021): Subsurface geological, hydrogeophysical and engineering characterisation of Etioro-Akoko, southwestern Nigeria, using electrical resistivity tomography, *NRIAG J. Astron. Geophys.*, **10**, 43–57, <https://doi.org/10.1080/20909977.2020.1868659>.
- Akingboye, A. S., Osazuwa, I. B. and Mohammed, M. Z. (2020): Electrical resistivity tomography for geoenvironmental investigation of subsurface defects: A case study of Etioro-Akoko highway, Ondo State, Southwestern Nigeria, *Studia Quaternaria*, **37**, 101–107, <https://doi.org/10.24425/sq.2020.133754>.
- Akingboye, A. S. and Ogunyele, A. C. (2019): Insight into seismic refraction and electrical resistivity tomography techniques in subsurface investigations, *Rudarsko-geološko-naftni Zbornik*, **34**, 93–111.
- Akintorinwa, O. J., Atitebi, M. O. and Akinlalu, A. A. (2020): Hydrogeophysical and aquifer vulnerability zonation of a typical basement complex terrain: A case study of Odode Idanre southwestern Nigeria, *Heliyon*, **6**, e04549, <https://doi.org/10.1016/j.heliyon.2020.e04549>.
- Arora, T., Boisson, A. and Ahmed, S. (2016): Non-intrusive hydro-geophysical characterization of the unsaturated zone of South India – A case study, *J. Afr. Earth Sci.*, **122**, 88–97, <https://doi.org/10.1016/j.jafrearsci.2016.04.021>.

- Bery, A. A. (2016): Slope monitoring study using soil mechanics properties and 4-D electrical resistivity tomography methods, *Soil Mech. Found. Eng.*, **53**, 24–29, <https://doi.org/10.1007/s11204-016-9359-7>.
- Bery, A. A. and Saad, R. (2012): Tropical clayey sand soil's behaviour analysis and its empirical correlations via geophysics electrical resistivity method and engineering soil characterizations, *Int. J. Geosci.*, **3**, 111–116, <https://dx.doi.org/10.4236/ijg.2012.31013>.
- bin Kamaruzzaman, M. Y., bin Zakariah, M. N. A. and Fudholi, A. (2020): Regional gravity study of Perak, Malaysia using satellite acquired data, *ARPJ. Eng. App. Sci.*, **15**, 1988–1993.
- Cao, J., Yang, X., Du, G. and Li, H. (2020): Genesis and tectonic setting of the Malaysian Waterfall granites and tin deposit: Constraints from LA–ICP (MC)–MS zircon U–Pb and cassiterite dating and Sr–Nd–Hf isotopes, *Ore Geol. Rev.*, **118**, 103336, <https://doi.org/10.1016/j.oregeorev.2020.103336>.
- Chalikakis, K., Plagnes, V., Guerin, R., Valois, R. and Bosch, F. P. (2011): Contribution of geophysical methods to karst-system exploration: An overview, *Hydrogeol. J.*, **19**, 1169–1180, <https://doi.org/10.1007/s10040-011-0746-x>.
- Cheng, Q., Tao, M., Chen, X. and Binley, A. (2019): Evaluation of electrical resistivity tomography (ERT) for mapping the soil–rock interface in karstic environments, *Environ. Earth Sci.*, **78**, 1–14, <https://doi.org/10.1007/s12665-019-8440-8>.
- Christensen, C. W., Hayashi, M. and Bentley, L. R. (2020): Hydrogeological characterization of an alpine aquifer system in the Canadian Rocky Mountains, *Hydrogeol. J.*, **28**, 1871–1890, <https://doi.org/10.1007/s10040-020-02153-7>.
- Dahlin, T. and Loke, M. H. (2018): Underwater ERT surveying in water with resistivity layering with example of application to site investigation for a rock tunnel in central Stockholm, *Near Surf. Geophys.*, **16**, 230–237, <https://doi.org/10.3997/1873-0604.2018007>.
- DeGroot-Hedlin, C. and Constable, S. (1990): Occam's inversion to generate smooth, two-dimensional models from magnetotelluric data, *Geophysics*, **55**, 1613–1624, <https://doi.org/10.1190/1.1442813>.
- Eriksson, L. O. (2014): Soil rock interfaces: Problem identification and conceptualisation for sealing strategies, M. Sc. Thesis submitted to the Department of Civil and Environmental Engineering Division of the Engineering Geology Research Group, Chalmers University of Technology, 123 pp.
- Ganerød, G. V., Rønning, J. S., Dalsegg, E., Elvebakk, H., Holmøy, K., Nilsen, B. and Braathen, A. (2006): Comparison of geophysical methods for sub-surface mapping of faults and fracture zones in a section of the Viggja road tunnel, Norway, *B. Eng. Geol. Env.*, **65**, 231–243, <https://doi.org/10.1007/s10064-006-0041-6>.
- Gao, Q., Shang, Y., Hasan, M., Jin, W. and Yang, P. (2018): Evaluation of a Weathered Rock Aquifer using ERT method in South Guangdong, China, *Water-Sui*, **10**, 293, <https://doi.org/10.3390/w10030293>.
- Hasan, M., Shang, Y., Jin, W. and Akhter, G. (2022): Site suitability for engineering-infrastructure (EI) development and groundwater exploitation using integrated geophysical approach in Guangdong, China, *B. Eng. Geol. Env.*, **81**, 7, <https://doi.org/10.1007/s10064-021-02503-z>.
- Hasan, M., Shang, Y., Akhter, G. and Jin, W. (2020): Delineation of contaminated aquifers using integrated geophysical methods in Northeast Punjab, Pakistan, *Environ. Monit. Assess.*, **192**, <https://doi.org/10.1007/s10661-019-7941-y>.
- Laloy, E., Javaux, M., Vanclooster, M., Roisin, C. and Biielders, C. L. (2011): Electrical resistivity in a loamy soil: Identification of the appropriate pedo-electrical model, *Vadose Zone J.*, **10**, 1023–1033, <https://doi.org/10.2136/vzj2010.0095>.
- Lee, C. P., Leman, M. S., Hassan, K., Nasib, B. M. and Karim, R. (2004): *Stratigraphic Lexicon of Malaysia*.
- Loke, M. H. (2004): Rapid 2D resistivity and IP inversion using the least-square method – Geoelectrical Imaging 2-D and 3D.

- Loke, M. H. and Lane, J. W. (2004): Inversion of data from electrical resistivity imaging surveys in water-covered areas, *Explor. Geophys.*, **35**, 266–271, <https://doi.org/10.1071/EG04266>.
- Loke, M. H. and Barker, R. D. (1996): Practical techniques for 3D resistivity surveys and data inversion, *Geophys. Prospect.*, **44**, 499–523, <https://doi.org/10.1111/j.1365-2478.1996.tb00162.x>.
- Metcalf, I. (2001): The Bentong-Raub Suture Zone, permo-triassic orogenesis and amalgamation of the Sibumasu and Indochina Terranes, *Gondwana Res.*, **4**, 700–701, [https://doi.org/10.1016/S1342-937X\(05\)70498-6](https://doi.org/10.1016/S1342-937X(05)70498-6).
- Metcalf, I. (2000): The Bentong-Raub Suture Zone, *J. Asian Earth Sci.*, **18**, 691–712, [https://doi.org/10.1016/S1367-9120\(00\)00043-2](https://doi.org/10.1016/S1367-9120(00)00043-2).
- Ng, S. W.-P., Chung, S.-L. L., Robb, L. J., Searle, M. P., Ghani, A. A., Whitehouse, M. J., Oliver, G. J. H., Sone, M., Gardiner, N. J. and Roselee, M. H. (2015a): Petrogenesis of Malaysian granitoids in the Southeast Asian tin belt: Part 1. Geochemical and Sr-Nd isotopic characteristics, *Geol. Soc. Am. Bull.*, **127**, 1209–1237, <https://doi.org/10.1130/B31213.1>.
- Ng, S. W.-P., Whitehouse, M. J., Searle, M. P., Robb, L. J., Ghani, A. A., Chung, S.-L., Oliver, G. J. H., Sone, M., Gardiner, N. J. and Roselee, M. H. (2015b): Petrogenesis of Malaysian granitoids in the Southeast Asian tin belt: Part 2. U-Pb zircon geochronology and tectonic model, *Geol. Soc. Am. Bull.*, **127**, 1238–1258, <https://doi.org/10.1130/B31214.1>.
- Nuhu, H., Hashim, S., Aziz Saleh, M., Syazwan Mohd Sanusi, M., Hussein Alomari, A., Jamal, M. H., Abdullah, R. A. and Hassan, S. A. (2021): Soil gas radon and soil permeability assessment: Mapping radon risk areas in Perak State, Malaysia, *PLOS ONE*, **16**, e0254099, <https://doi.org/10.1371/journal.pone.0254099>.
- Robineau, B., Join, J. L., Beauvais, A., Parisot, J.-C. and Savin, C. (2007): Geoelectrical imaging of a thick regolith developed on ultramafic rocks: Groundwater influence, *Aust. J. Earth Sci.*, **54**, 773–781, <https://doi.org/10.1080/08120090701305277>.
- Schwartz, M. O., Rajah, S. S., Askury, A. K., Putthapiban, P. and Djaswadi, S. (1995): The Southeast Asian tin belt, *Earth Sci. Rev.*, **38**, 95–293, [https://doi.org/10.1016/0012-8252\(95\)00004-T](https://doi.org/10.1016/0012-8252(95)00004-T).
- Soupios, P. M., Georgakopoulos, P., Papadopoulos, N., Saltas, V., Andreadakis, A., Vallianatos, F., Sarris, A. and Makris, J. P. (2007): Use of engineering geophysics to investigate a site for a building foundation, *J. Geophys. Eng.*, **4**, 94–103, <https://doi.org/10.1088/1742-2132/4/1/011>.
- Stober, I. and Bucher, K. (2015a): Hydraulic conductivity of fractured upper crust: Insights from hydraulic tests in boreholes and fluid-rock interaction in crystalline basement rocks, *Geofluids*, **15**, 161–178, <https://doi.org/10.1111/gff.12104>.
- Stober, I. and Bucher, K. (2015b): Hydraulic and hydrochemical properties of deep sedimentary reservoirs of the Upper Rhine Graben, Europe, *Geofluids*, **15**, 464–482, <https://doi.org/10.1111/gff.12122>.
- Storz, H., Storz, W. and Jacobs, F. (2000): Electrical resistivity tomography to investigate geological structures of the earth's upper crust, *Geophys. Prospect.*, **48**, 455–471, <https://doi.org/10.1046/j.1365-2478.2000.00196.x>.
- Tate, R. B., Tan, D. N. K. and Ng, T. F. (2009): Geological Map of Peninsular Malaysia, in: *Geology of Peninsular Malaysia* edited by Hutchison, C. S. and Tan, D. N. K. University of Malaya/Geological Society of Malaysia, Kuala Lumpur.
- Yalcinkaya, E., Alp, H., Ozel, O., Gorgun, E., Martino, S., Lenti, L., Bourdeau, C., Bigarre, P. and Coccia, S. (2016): Near-surface geophysical methods for investigating the Buyukcekmece landslide in Istanbul, Turkey, *J. App. Geophys.*, **134**, 23–35, <https://doi.org/10.1016/j.jappgeo.2016.08.012>.
- Yang, X., Wang, Y. and Sun, Z. (2020): The shearing anisotropy characteristics on the interface of loess with bedrock, *B. Eng. Geol. Environ.*, **79**, 5205–5212, <https://doi.org/10.1016/j.oceaneng.2016.11.013>.

SAŽETAK

Kartiranje dubine osnovne stijene u granitnom okruženju kombiniranjem metode električne tomografije i bušotinskih podataka*Adedibu Sunny Akingboye i Andy Anderson Bery*

U ovoj studiji korišteni su električna tomografija (ERT) i bušotinski podatci za kartiranje dubine osnovne stijene ispod četiri profila (RS1, RS2, RS3 i RS4) u granitnom terenu Peraka, poluotoka Malezije. Cilj studije bio je procijeniti utjecaje karakterističnih značajki dubine osnovne stijene na podzemne vode i razvoj infrastrukture kako bi se zadovoljile potrebe godišnjeg porasta broja stanovnika. Litološke jedinice izvedene iz bušotinskih zapisa i ERT-a snažno su povezane. Određene litološke jedinice uključuju gornji sloj tla, istrošene granitne jedinice (srednje čvrsta do tvrda muljevita glina ili glinasti mulj s $\rho < 800 \Omega\text{m}$), tanke do široke istrošene/raspucane jedinice i svježu granitnu podlogu. Ovakvi profili tlo-stijena i istrošeni/raspucani otvori podržavaju održivi razvoj podzemnih voda s dubinama bušenja iznad 45 m. Nasuprot tome, utvrđeni slojevi gline/mulja koji se izmjenjuju s tvrdim tlima, zonama s duboko istrošenim/raspucanim stijenama slabe nosivosti i gromadama osnovne stijene na većini mjesta, osim ispod profila RS3, imaju velike sklonosti za zadržavanje vode i diferencijalna naprezanja. Ove značajke mogu negativno utjecati na loše ojačane temelje. Stoga, konstruktivne elemente temelja, kao što su podnožja ili piloti, treba postaviti na stabilnu stijensku podlogu, posebno u središnjem do zapadnom dijelu istraživanog područja. Ovo je istraživanje smanjilo nedostatak informacija o korištenju metode ERT i bušotinskih podataka u istraživanjima dubine osnovne stijene u razmatranom području.

Ključne riječi: otpornost na granici tla i stijene, bušotinski podatci, granica tlo-stijena, granitno područje, hidrogeofizika, geoinženjersko istraživanje

Corresponding authors' addresses:

Adedibu Sunny Akingboye, School of Physics, Universiti Sains Malaysia, 11800 Penang, Malaysia; Department of Earth Sciences, Adekunle Ajasin University, 001 Akungba-Akoko, Ondo State, Nigeria; e-mail: adedibu.akingboye@aau.edu.ng

Andy Anderson Bery, School of Physics, Universiti Sains Malaysia, 11800 Penang, Malaysia; e-mail: andersonbery@usm.my



This work is licensed under a Creative Commons Attribution-NonCommercial 4.0 International License.